Testing models of accreting stars in massive binaries on ζ Ophiuchi

M. Renzo[1, 2] and Y. Götberg[3]

[1]*Department of Physics, Columbia University, New York, NY 10027, USA*
[2]*Center for Computational Astrophysics, Flatiron Institute, New York, NY 10010, USA*
[3]*The Observatories of the Carnegie Institution for Science, 813 Santa Barbara Street, Pasadena, CA 91101, USA*

ABSTRACT

Binarity dominates the evolution of massive stars, and the nearest O-type star to Earth, ζ Ophiuchi, has long been proposed to be a product of binary evolution. Despite this, most stellar models have tried unsuccessfully to reproduce its observable properties relying on single-star rotating models. ■ [Here we do better] ■

Keywords: stars: individual: ζ Ophiuchi – stars: massive – stars: binaries

1. INTRODUCTION

The overwhelming majority of massive stars is born in multiple systems (e.g., Mason et al. 2009; Almeida et al. 2017), and a large fraction will exchange mass or merge with a companion in their lifetime (e.g., Sana et al. 2012). The most common type of interaction is a post-main-sequence stable mass transfer (case B) through Roche Lobe overflow (RLOF, Kippenhahn & Weigert 1967). Many studies (e.g., Götberg et al. 2017, 2018; Laplace et al. 2020, 2021; Blagorodnova et al. 2021) ■ [more refs. from other groups] ■ have focused on the dramatic impact of these interactions on the initially more massive donor star. Often the closest binary companion is treated as a point mass.

However, binary interactions have a crucial impact on the initially less massive star too: during mass transfer, these are expected to accrete mass, spin up to critical rotation (e.g., Packet 1981; Cantiello et al. 2007), and possibly be polluted by CNO-processed material from the inner core of the donor star (e.g., Blaauw 1993). The growth of the convective core due to the increased mass leads to "rejuvenation" of the accretor (e.g., Neo et al. 1977; Schneider et al. 2016).

Understanding the evolution of accretors in massive binaries has wider and crucial implications for stellar populations, electromagnetic transient observations, and gravitational-wave progenitors. Accretors (and mergers) can appear as blue stragglers and thus impact cluster populations and their age estimates and main sequence morphology (e.g., Pols & Marinus 1994; Wang et al. 2020). Moreover, the majority of massive binaries will be disrupted by the first supernova ejecting the companion ("binary SN scenario", Blaauw 1961; De Donder et al. 1997; Eldridge et al. 2011; Renzo et al.

2019; Evans et al. 2020). Therefore, populations of field massive stars contain presently single O-type stars that accreted mass earlier on. The majority of these will be too slow to stand out in astrometric surveys (e.g., Eldridge et al. 2011; Renzo et al. 2019). Assuming a constant star formation history, Renzo et al. (2019) estimated that $10.1^{+4.6}_{-8.6}\%$ of O-type stars might be accretors released after a SN – where the errors span a range of parameter variations.

From the transients perspective, massive accretors stars are also important: Zapartas et al. (2019) showed that $14^{+4}_{-11}\%$ of hydrogen-rich (type II) SNe might come from these progenitors after being ejected from a binary. The fact that they accreted mass before exploding can influence their helium (He) core mass and thus the explosion properties and the inferred progenitors (Zapartas et al. 2021).

Finally, the majority of isolated binary evolutionary scenarios for gravitational-wave progenitors go through a common-envelope phase initiated by the originally less massive accretor after the formation of the first compact object (e.g., Belczynski et al. 2016; Tauris et al. 2017; Broekgaarden et al. 2021). Therefore, it is possible that accretion of mass before the formation of the first compact object could modify the internal structure of the star that will initiate the common-envelope phase (e.g. Law-Smith et al. 2020; Klencki et al. 2021).

Despite their importance, accretor stars in binaries have so far received much less attention than the donor stars, with the pioneering studies of Ulrich & Burger (1976); Hellings (1983, 1984), and Braun & Langer (1995) as notable exceptions. Large grids of accretor models are lacking, most of the studies focus on lower mass B-type donors (e.g., van Rensbergen et al. 2006, 2011, but see also Wang et al. 2020) and only few sparse

massive models exist (e.g., Cantiello et al. 2007). This is because of the complexity of modeling these, which requires following in detail the *coupled* evolution of two rotating stars exchanging mass. Moreover, the admittedly large number of free parameters involved in the modeling of each individual star and their interactions makes robust predictions challenging to obtain. Here, we argue that the nearest O-type star to Earth, ζ Ophiuchi[1] (ζ Oph) provides a unique opportunity to constrain these models.

ζ Oph has a distance from Earth of $107 \pm 4\,\mathrm{pc}$ (Neuhäuser et al. 2020, and references therein), and a spectral type O9.5IVnn (Sota et al. 2014). It occasionally shows emission lines (Walker et al. 1979; Vink et al. 2009), making it an Oe star. It was originally identified as a runaway because of its large proper motion by Blaauw (1952). Unfortunately, the *Gaia* data for this object are not of sufficient quality[2] to improve previous astrometric results, but estimates of the peculiar velocity range in $30 - 50\,\mathrm{km\ s^{-1}}$ (e.g., Zehe et al. 2018; Neuhäuser et al. 2020). The large velocity with respect the surrounding interstellar material is also confirmed by the presence of a prominent bow-shock (e.g., Bodensteiner et al. 2018).

Because of its young apparent age, extremely fast rotation ($v\sin(i) \gtrsim 400\,\mathrm{km\ s^{-1}}$, e.g., Zehe et al. 2018), and nitrogen (N) and He rich surface (e.g., Herrero et al. 1992; Blaauw 1993; Villamariz & Herrero 2005; Marcolino et al. 2009), ζ Oph is a prime candidate for the binary SN scenario (Blaauw 1993). Many studies have suggested ζ Oph might have accreted mass from a companion before acquiring its large velocity, both from spectroscopic and kinematic considerations (e.g., Blaauw 1993; Hoogerwerf et al. 2000, 2001; Tetzlaff et al. 2010; Neuhäuser et al. 2020) and using stellar modeling arguments (e.g., van Rensbergen et al. 1996). Recently, Neuhäuser et al. (2020) suggested that $1.78 \pm 0.21\,\mathrm{Myr}$ ago a supernova in Upper-Centaurus-Lupus produced the pulsar PSR B1706-16, ejected ζ Oph, and also injected the short-lived radioactive isotope $^{60}\mathrm{Fe}$ on Earth. This argues strongly for a successful supernova explosion of the companion with a large $\sim 250\,\mathrm{km\ s^{-1}}$ natal kick, which in most cases would be sufficient to disrupt the binary (e.g., Tauris 2015; Renzo et al. 2019; Evans et al. 2020).

Although the nature of ζ Oph as a binary product is well established, because of its observed large surface rotation rate, previous attempts to model it rely purely

on rotational mixing to explain the surface composition (e.g., Maeder & Meynet 2000). Even the binary models of van Rensbergen et al. (1996) assumed spin-up due to mass accretion to drive rotational mixing from the interior of the accreting star (see also Cantiello et al. 2007). However, Villamariz & Herrero (2005) (hereafter, VH05) were unable to find good fit for the stellar spectra using the rotating models from Meynet & Maeder (2000).

This may not be surprising: rotational mixing has lower efficiency for metal-rich and relatively low mass stars because of the increased importance of mean molecular weight gradients and longer thermal timescales compared to more massive stars (e.g., Yoon et al. 2006; Perna et al. 2014). The parent association has a metallicity $Z = 0.01 \simeq Z_\odot$ (based on asteroseismology from Murphy et al. 2021), and mass estimates for ζ Oph range from $13 - 25\,M_\odot$, at the lower end of the range where efficient mixing might bring He and CNO-processed material to the surface (chemically homogeneous evolution).

Given the challenges in explaining the surface composition of ζ Oph with rotational mixing from the stellar interior and the strong evidence for its past as a member of a binary system, this star offers a unique opportunity to constrain the evolution of accreting stars in massive binary systems.

Here, we present self-consistent binary evolution models for ζ Oph computing simultaneously the coupled evolution of *both* donor and accretor star and their orbit. ■ [fix order description] ■ After presenting our `MESA` setup in Sec. 2, we show our best model which reproduces the majority of the salient features of this star in Sec. 3. We discuss the sensitivity of our results to the admittedly many free parameters required for this kind of computations in Sec. **??**. Finally, we conclude in Sec. 5.

2. MODELING MASSIVE BINARIES WITH `MESA`

Modeling the evolution of massive binaries ($M_1 \gtrsim 20\,M_\odot \geq M_2$) is challenging because of the intricate role of several notoriously difficult stellar physics ingredients (differential rotation, mixing, high mass-loss rates, accretion, etc.). Here we follow self-consistently the coupled evolution of two massive stars in a binary system using `MESA` (version 15140). Our choice of input parameters and our numerical results are available at ■ [link] ■. We discuss here only the main relevant physical parameters, and Appendix A gives more details on our choice of input physics.

We adopt the Ledoux criterion to determine convective stability and a mixing length parameter of 1.5. We include semiconvection and thermohaline mixing follow-

---

[1] also known as HD 149 757.

[2] The renormalized unit weighted error (RUWE) of this star in Gaia EDR3 is 4.48.

ing Langer et al. (1983) and Kippenhahn et al. (1980), respectively, each with efficiency 1.0. We use the exponential core overshooting from Herwig (2000) with free parameters $(f, f_0) = (4.25 \times 10^{-2}, 10^{-3})$ (Claret & Torres 2017) which broadly reproduce the width of the main sequence from Brott et al. (2011). We also use the local implicit enhancement of the convective flux in superadiabatic regions (`MLT--`) introduced in `MESA 15140`.

We treat rotation in the "shellular" approximation and initialize it assuming tidal synchronization at the beginning of the evolution. For our fiducial period choice ($P = 100$ days), this effectively means both the stars in our binary are initially slow rotators. Our models include in a diffusive approximation the effect of Eddington-Sweet circulations (Sweet 1950), which dominates the chemical mixing due to rotation. We also include the secular and dynamical shear instabilities, and the Goldreich-Schubert-Fricke instability as in Götberg et al. (2017, 2018); Laplace et al. (2020, 2021). We assume a Spruit-Tayler dynamo for the transport of angular momentum (Spruit 2002), and chose the same free parameters as Heger et al. (2000). This also includes the rotational enhancement of wind mass loss as in Langer (1998).

We assume a fiducial metallicity of $Z = 0.01$ informed by the present-day Z of the parent cluster (Murphy et al. 2021), and assume scaling of the relative element abundances with the solar abundances of Grevesse & Sauval (1998). We include wind mass loss with the Vink et al. (2000, 2001) hot wind, and de Jager et al. (1988) for effective temperature $T_{\rm eff} < 10^{4.2}$ K, both with a scaling factor of 1. Nominally, this means our wind mass-loss rate post-mass transfer is overestimated by almost a factor of 100 compared to observations (weak wind problem, see Marcolino et al. 2009). However, Lucy (2012) and Lagae et al. (2021) proposed that the temperature structure of the winds of low-luminosity O-type stars might affect the spectral lines and cause an empirical underestimate of the mass-loss rate.

Both stars are evolved simultaneously on the same timesteps until after the donor detaches from its Roche lobe. We follow Kolb & Ritter (1990) to calculate the mass transfer rate from optically thick layers of the donor star during Roche lobe overflow (RLOF). Moreover, we assume that the transfered layers reach the accretor with the accretor's specific surface angular momentum and entropy, but the chemical composition is determined by the inner evolution of the donor star. Mass transfer is conservative until the accretor reaches critical rotation, after which rotationally enhanced mass loss governs the accretion efficiency.
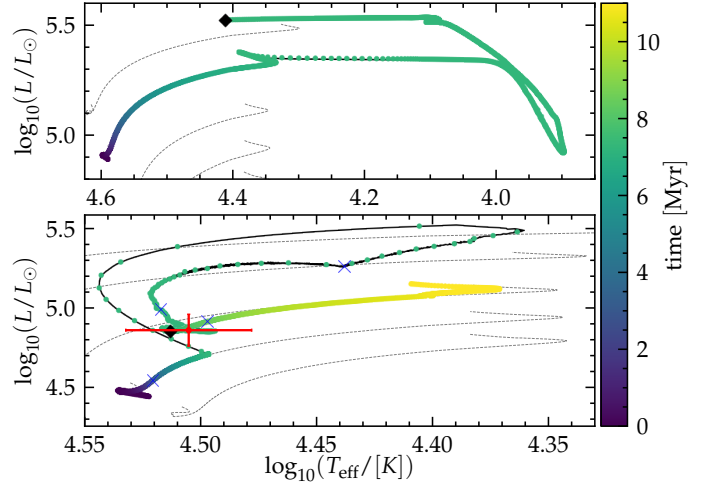
Figure 1. HRD for the donor star (top) and accretor star (bottom) of the progenitor binary of ζ Oph. Each point is separated by 50 years of evolution. The colors represent the stellar age, the red datapoint shows the position of ζ Oph according to VH05, thin blue crosses mark the position of the profiles shown in Fig. 3, and the black diamonds mark the position at the end of the binary run. We continue the accretor evolution as a single star from there until core H depletion, hence the bottom panel shows a longer time. We emphasize the different scales on the two panels. The thin gray dashed line show the main sequence evolution of nonrotating single stars of 15, 17, 25, and 30 $M_\odot$ at $Z = 0.01$ for comparison.

To define RLOF detachment, we take advantage of the fact that we focus here on case B interactions among massive stars. After losing their envelope, massive donors are not expected to expand to hundreds of $R_\odot$ during He shell burning at the metallicity we consider (e.g., Laplace et al. 2020). Thus, we define RLOF detachment as the moment after the onset of RLOF when the donor has a surface He mass fraction larger than 0.35 (indicating that a significant amount of envelope has been lost or transferred), a radius smaller than its terminal-age main sequence (TAMS, defined as when the central mass fraction of H drops below 10^4) radius, and no mass is being transferred anymore. At this point in time, we save a model for the accreting star, and continue its evolution as a single star until TAMS with the same setup.

■ [describe parameter variations in this sec.] ■

3. MASSIVE BINARY EVOLUTION NATURALLY EXPLAINS ζ OPHIUCHI'S PROPERTIES

We describe here the evolution of a binary system where the accretor star can broadly reproduce all the observed features of ζ Oph. We assume initial masses

$M_1 = 25\,M_\odot$, $M_2 = 17\,M_\odot$ on a period of 100 days at $Z = 0.01$.

Fig. 1 shows the Hertzsprung-Russell diagrams (HRD) of both stars. After $\sim$7.24 Myr, the donor star (top panel) evolves off the main sequence and $\sim$ 8400 years later, when the donor's effective temperature reaches about $T_{\rm eff} \simeq 10^4\,{\rm K}$, mass transfer starts. This results in a stable case B RLOF. We refer to Götberg et al. (2017); Laplace et al. (2021); Blagorodnova et al. (2021) and references therein for a detailed description of the evolution of massive donor stars in binaries. Although our models are more massive, the qualitative behavior of the donor star is similar.

At the onset of RLOF, the accretor star (bottom panel of Fig. 1) is still on the main sequence with $T_{\rm eff} \simeq 10^{4.5}$ K. Because of accretion, it quickly becomes over-luminous ($L \simeq 10^{5.4}\,L_\odot$), and its radius increases dramatically from $\sim 7.5\,R_\odot$ to $\sim 35\,R_\odot$. Once the accretor reaches critical rotation (roughly at the lowest $T_{\rm eff}$ in the bottom panel of Fig. 1), the star begins contracting and its $T_{\rm eff}$ increases. At $T_{\rm eff} \simeq 4.43$ K the material transferred from the companion star becomes progressively more He-rich, causing a "v-shaped" feature in the evolutionary track. This indicates that the partially processed outer layers of the donor's core are uncovered by mass transfer. This late mass transfer puts material at high mean molecular weight μ on top of the primordial envelope of the accretor, modifying the morphology of the evolutionary track. Thermohaline mixing starts in the outer layers of the accreting star, and, together with rotational mixing, it progressively dilutes the surface He and N mass fractions and causes noisy features on the HR diagram (e.g., Cantiello et al. 2007). Sec. 3.1 describes in more detail the mixing processes inside the accretor, we emphasize here that the algorithmic choices made to model mixing (and rotation) might impact the morphology of the accretor's evolutionary track during RLOF. However, the entire duration of RLOF (and thus of the feature in the bottom panel of Fig. 1 from the departure from the main-sequence to the black diamond) is only about 10^4 years.

We evolve the binary system until the black diamonds in Fig. 1, which occurs well after the donor detaches from the Roche Lobe. At this point, the accretor is a H-rich fast-rotating star of $\sim$20.1 $M_\odot$. Available mass estimates for the presently single ζ Oph are highly uncertain, but most include 20 $M_\odot$ (e.g., Hoogerwerf et al. 2001, VH05, Neuhäuser et al. 2020). The accretor's post-RLOF orbital velocity is $v_2 \simeq 40\,{\rm km\,s^{-1}}$, which is expected to decrease a bit further due to wind-driven widening of the binary, but is in good agreement with the presently observed runaway velocity of ζ Oph.

Accounting for both wind mass loss and the amount of mass transferred, at the end of RLOF the donor becomes a He star of $\sim$9.4 $M_\odot$, likely to contract further and appear as a Wolf-Rayet star. It's surface H mass fraction is $\lesssim 0.2$ and most of the H is likely to be removed by further wind mass loss (e.g., Götberg et al. 2017). ■ [Ylva: want to expand?] ■. ■ [maybe move next paragraph to discussion?] ■ For our assumed scenario to work, such donor needs to successfully explode in a SN, breaking the binary system and making a neutron star remnant. While the post-RLOF donor mass we obtain is rather high, recent studies suggest higher "explodability" of donor stars in binary systems (e.g., Schneider et al. 2021; Laplace et al. 2021; ?). Furthermore, neither the initial donor mass M_1 nor the initial period are observable, and thus there is room to chose different values to obtain easier to explode donors and faster (or slower) accretors post-RLOF.

From the black diamond onwards, we evolve the accretor as a single star with the same MESA setup until TAMS. The main-sequence track on which the accretor settles post-RLOF has a higher luminosity compared to the original track because of the accretion of mass, and it has also a slightly different slope due to the close-to-critical rotation and the accretion of partially nuclearly processed material (He- and N-rich) material.

The red errorbars in the bottom panel of Fig. 1 mark the approximate position of ζ Oph based on the analysis of VH05. The color of the track in Fig. 1 indicate that our accreting star spends about $\sim$2 Myr within the represented errorbars after the end of RLOF. Assuming the kinematic age of 1.78 ± 0.21 (Neuhäuser et al. 2020), and estimating a remaining lifetime of the donor of $\sim$0.5 Myr, this gives the correct timescale for the binary SN scenario. The observed position of ζ Oph on the HRD, and especially its relatively high $T_{\rm eff}$ would be hard to reproduce assuming initially less massive accretors (which would remain too cool even after accreting mass), or more equal initial mass ratio (which would produce a too evolved accretor at the onset of mass transfer).

Fig. 2 shows the rate of mass change for each star during RLOF. The top panel focuses on the donor star which loses mass to RLOF (cyan line) and wind mass loss (thin red line). The dashed blue lines show their combination resulting in the actual rate of mass change of the stars. The bottom panel shows instead the accreting star, which grows in mass because of the mass transfer. At peak the mass transfer rates reaches very high values above $10^{-2.5}\,M_\odot\,{\rm yr^{-1}}$, and taps into the optically thick matter of the donor.
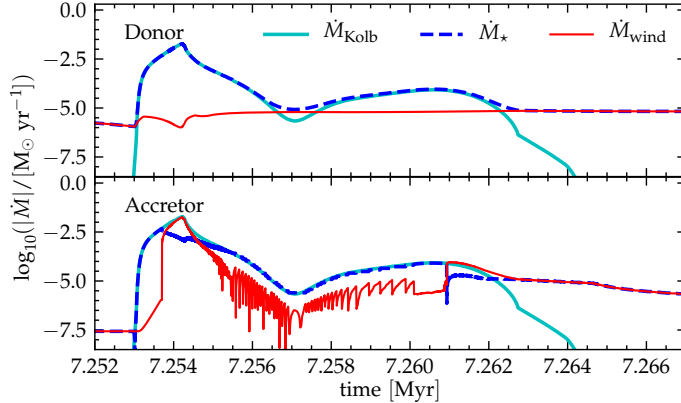
Figure 2. Mass transfer rates as a function of time during RLOF. The top (bottom) panel shows the donor (accretor) star. The cyan solid lines show the mass transfer rate between the two stars. The dashed blue lines show the actual change in the mass of the stars (due to the combination of wind, and accretion efficiency). The thin red lines show the wind mass loss rates. During RLOF the accretor reaches critical rotation, which leads to oscillations in the rotationally-enhahnced wind mass loss.

At the end of RLOF, the donor star briefly expands again ($T_{\rm eff} \simeq 10^{4.1}$ K, $L \simeq 10^{5.5} L_\odot$). This is due to the partial recombination of the now He-rich outer layers, which causes a transient surface convection layer. This causes the second broad peak in the mass transfer rates centered at 7.261 Myrs. We find this to be the culprit of difficulties in modeling massive binaries transferring mass in older `MESA` releases, because although only a very small amount of mass is involved, this would lead to large radial expansion much beyond the donor's Roche lobe, and cause numerical problems.

The wind mass loss (in red) controls the accretion efficiency and thus the difference between the actual rate of change in mass of the accretor (thick dashed blue) and the rate at which mass is being transferred. At peak, where the red and the cyan lines overlap, mass transfer becomes very non-conservative, but for most of the evolution the (rotationally enhanced) wind removes only a fraction of the accreted mass. The interplay between the stellar radius and rotation causes the oscillations visible in the bottom panel, whose amplitude is generally lower than the RLOF mass transfer rate.

3.1. *Mixing and composition*

`MESA` treats mixing processes in the diffusion approximation (Paxton et al. 2011). To illustrate the dominant processes throughout the accretor's evolution, we show in Fig. 3 the diffusion coefficients for various mixing processes as a function of mass coordinate at selected times. Each panel corresponds to one of the thin blue crosses in the bottom panel of Fig. 1, and the gray shaded ar-

eas mark mass accreted during RLOF. The last panel roughly represents the predicted internal structure of ζ Oph as observed today.

In Fig. 3, the thin red lines correspond to convection, with the initial convective core of $\sim 6\,M_\odot$ clearly visible in the first panel. In all models, a tiny sub-surface convective region is also visible in the outermost layers (see e.g., Cantiello et al. 2021). The thin blue lines mark mixing processes that are not related to rotation, nor are any of the other processes explicitly shown, which here effectively means overshooting. The extension of the diffusion coefficient above the convective core in all panels is the typical behavior for an exponentially decreasing overshooting. Purple and pink represent semiconvection and thermohaline mixing, respectively. Before mass transfer (left-most panel), only a small amount of sub-surface thermohaline mixing occurs, with a mass extent comparable or smaller to the sub-surface convective zone, and no semiconvection occurs. The thick cyan line corresponds to the total diffusion coefficient, obtained as the sum of the diffusion coefficients for each process modeled: where the cyan line is not overlapping with the others, rotational mixing (and more specifically Eddington-Sweet meridional circulation) is the dominant process.

During RLOF (second and third panel), the spin-up due to accretion causes an increase in the rotational mixing (see also Sec. 3.2), and the accretion of nuclearly processed material progressively widens the thermohaline mixing region at the surface. Late during the mass transfer (third panel), thermohaline mixing dominates the outermost layers – except within the sub-surface convective zone, but throughout most of the envelope rotation does the lion's share of the mixing. Thermohaline mixing and Eddington-Sweet circulations together mix inwards and dilute the CNO-enriched material coming from the donor's surface.

At the same time, the increase in the accretor mass drives rejuvenation (e.g., Schneider et al. 2016). This can be seen as a growth of the convective core from $\sim 6\,M_\odot$ to almost $\sim 8\,M_\odot$, plus the corresponding growth of the overshooting region. This mixes inward H-rich material resulting in an elongation of the accretor's lifetime, and at the same time mixes outward CNO-equilibrium matter, connecting the N-rich core with the outer envelope polluted from the top.

Tab. 1 summarizes the surface properties of the accretor star at the time shown in the last panel of Fig. 3, that is shortly after the RLOF phase, while the model is still roughly at the observed position of ζ Oph.

Both the mass and radius agree reasonably well with the estimates from VH05 and previous studies, that
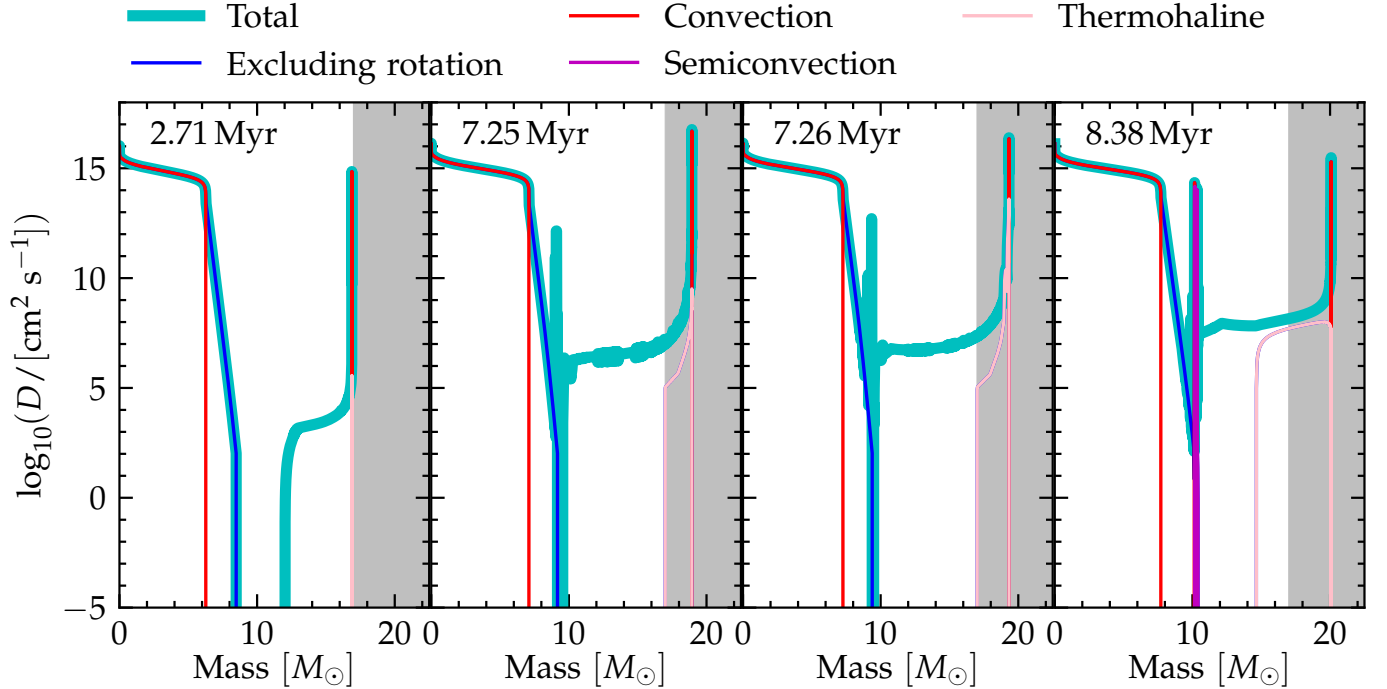
Figure 3. Mixing diffusion coefficients in the accretor star. From left to right, each panel shows times during the main sequence (2.71 Myr), right before the "v-shaped" feature during RLOF (7.25 Myr), close to the end of RLOF (7.26 Myr), and after mass transfer (8.38 Myr) – see the corresponding thin blue crosses in Fig. 1. The total diffusion coefficient (thick cyan line) is obtained as the sum of non-rotational mixing processes (i.e., here overshooting, thin blue line), convection (shown in red), thermohaline mixing (pink) and semiconvection (in purple). The gray area corresponds to mass accreted during RLOF.

M [$M_\odot$]	R [$R_\odot$]	$\log_{10}(\omega/[\mathrm{s}^{-1}])$	v_{rot} [km s^{-1}]	$X(^1\mathrm{H})$	$X(^4\mathrm{He})$	$X(^{12}\mathrm{C})$	$X(^{14}\mathrm{N})$	$X(^{16}\mathrm{O})$
20.1	9.6	-4.263	366.1	0.678010	0.312093	0.001344	0.001340	0.004148

Table 1. Properties of the accretors shortly after the end of RLOF (last thin blue cross in Fig. 1 and last panel of Fig. 3).

is $20\,M_\odot$ and $8.3 \pm 1.5\,R_\odot$, respectively. The surface rotational velocity in excess of $350\,\mathrm{km\,s^{-1}}$ is also in the correct ballpark albeit possibly on the low end. We report the surface H mass fraction[3], lower than primordial because of the accretion of nuclearly processed material, and the surface mass fraction of the most prominent species ^{4}He, ^{12}C, ^{14}N, ^{16}O. Assuming our surface H mass fraction $X(^1\mathrm{H})$, the corresponding mass fractions of ^{4}He, ^{12}C, ^{14}N, ^{16}O obtained by VH05 are $0.33^{+0.14}_{-0.05}$, 0.0006 ± 0.0004, 0.002 ± 0.001, and 0.005 ± 0.004. Our values are sensitive to the interplay between several poorly understood processes treated in one dimension: mass accretion efficiency, rotationally enhanced wind mass loss, thermohaline, and inward rotational mixing. Therefore, although not perfect, we consider the match with the

mass fractions reported by VH05 surprisingly satisfactory.

3.1.1. *Comparison to single fast-rotating stars*

We now compare the mixing processes happening in a single rotating massive stars and in our accretor model. Fig. 4 shows the mass fraction of ^{14}N as a function of mass coordinate along the evolution of three $20\,M_\odot$ stars initialized with $\omega/\omega_{\mathrm{crit}} = 0.2, 0.3, 0.4, 0.5$ where ω is the surface angular frequency and $\omega_{\mathrm{crit}} = \sqrt{(1 - L/L_{\mathrm{Edd}})GM/R^3}$ and L_{Edd} is the Eddington luminosity computed using the stellar opacity from the outermost mesh point down to optical depth $\tau = 2/3$, L is the luminosity, R the radius of the star, and G the gravitational constant. These rotating single stars have an otherwise identical setup as our binary model. The last panel of Fig. 4 shows our accretor model. The dotted red line marks the primordial mass fraction of ^{14}N for the adopted $Z = 0.01$, the thin dashed lines mark the surface value at TAMS.

---

[3] This is needed to convert mass fractions reported here into $\varepsilon(X) = 12 + \log_{10}(N_X/N_H)$, where N_X and N_H are the number fractions of species X and H, respectively.
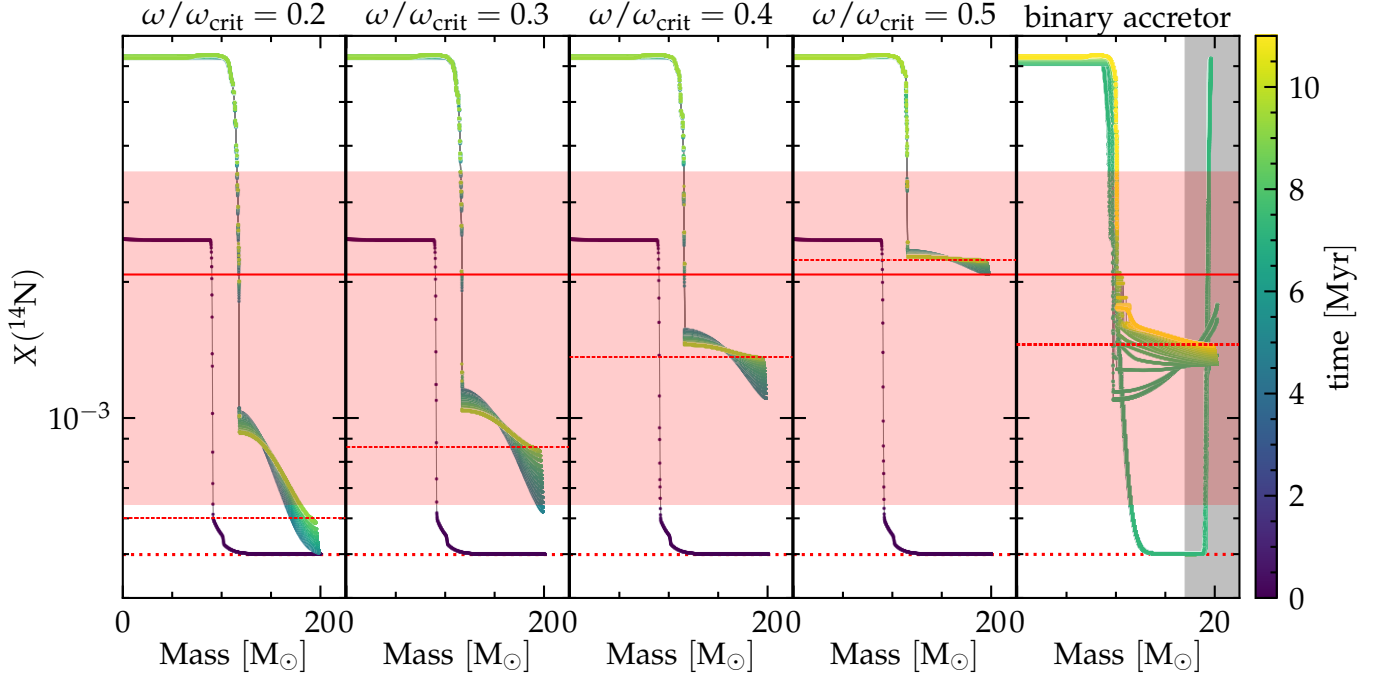
Figure 4. ^{14}N mass fraction as a function of mass coordinate for $20\,M_\odot$ single star models with increasing $\omega/\omega_{\rm crit}$ at birth (first four panels), and for the accretor of our fiducial binary. The dotted thick red line marks the primordial value, the thin dashed red line marks the surface value at TAMS. In the last panel, the gray area highlights mass accreted during RLOF. The colors of each profile go from dark to light at TAMS, and selected profiles along the main sequence are shown. The solid red line and the shaded red region correspond to the mass fraction of ^{14}N estimated by VH05 assuming the surface mass fraction of H from Tab. 1. The abundance of ^{14}N alone is not strongly constraining.

The colored tracks show selected profiles throughout the main sequence, with lighter colors corresponding to more evolved stars. The accretor model (rightmost panel) starts as a $17\,M_\odot$ and is rejuvenated by binary interactions, thus it reaches TAMS at $11.24\,{\rm Myr}$. For comparison, the initially $20\,M_\odot$ rotating models have a main-sequence lifetime of 9.2-$9.6\,{\rm Myr}$ (longer for higher initial rotation rates), hence their TAMS profile does not have as light a color in Fig. 4.

The first four panels of Fig. 4 show the typical rotational mixing profiles: ^{14}N rapidly rises in the core because of the CNO burning, and it is then mixed outwards. At any time the ^{14}N profile is monotonically decreasing in mass coordinate, and the higher the initial rotation, the higher the surface ^{14}N mass fraction reached at TAMS.

Conversely, the ^{14}N mass fraction profile of the accretor is *not* monotonic throughout the evolution. It is shaped not only by outward rotational mixing, but also by the accretion of matter from the outer layers of the donor's star core mixed inward by rotation and thermohaline mixing.

Initially, the tidally synced accretor star rotates too slowly for significant outward rotational mixing out of the core, and until the onset of RLOF (roughly at

$7.25\,{\rm Myr}$) no appreciable variation of the surface $X(^{14}{\rm N})$ occurs. During late RLOF after the "v-shaped" feature in Fig. 1, N-rich material from the donor's core piles onto the accretor's surface – inside the gray area in the rightmost panel of Fig. 4. The close-to-critical rotation of the accretor and the inversion in the mean molecular weight μ then drive inward mixing (see also Fig. 3) of this N-rich material and dilute it in the envelope.

Simultaneously, the mere growth in mass causes the steepening of the core-temperature gradient and increase in the convective core mass (rejuvenation, e.g., Schneider et al. 2016), driving some outward convective mixing of N-rich material. Because convection turnover timescales are much shorter than evolutionary timescales, the growth of the convective core produces "steps" at the outer edge of the core (slightly outside mass coordinate $10\,M_\odot$). In the post-RLOF evolution, outward rotational mixing from the rejuvenated core and inward rotational mixing and thermohaline mixing from the surface connect the excess ^{14}N.

In Fig. 4, the solid red line and red shaded area across all panels show the ^{14}N from VH05 (assuming the surface mass fraction from our model listed in Tab. 1): the mass fraction of ^{14}N alone is not sufficient to distinguish with these models, and already a moderate $\omega/\omega_{\rm crit} \geq 0.3$

is sufficient for models to reach the lower-limit of the error bar.

3.2. *Angular momentum transport and surface rotation*

One of the main distinguishing features of ζ Oph is its extremely high surface rotation rate. Spectroscopic measurements of the projected rotational velocity exceed $v\sin(i) \gtrsim 400\,\mathrm{km\,s^{-1}}$, which implies close to critical rotation. Zehe et al. (2018) recently estimated $v\sin(i) = 432 \pm 16\,\mathrm{km\,s^{-1}}$ and $i \sim 56$ degrees.

Fig. 5 shows the surface average rotation rate of our accretor model as a function of time (ignoring the projection angle i). The dark red band corresponds to the $v\sin(i)$ from Zehe et al. (2018), and the lighter band shows a range of 5 times their error bar.

The initial binary is wide enough that the initial tidal synchronization implies a very low rotation. At 7.25 Myr, RLOF rapidly spins up the accretor to critical rotation, up to $v_{\mathrm{crit}} \simeq 520\,\mathrm{km\,s^{-1}}$. The star remains fast rotating throughout the mass transfer phase, which ends at the black diamond in Fig. 5. In the remaining evolution, the star spins down progressively through wind mass loss, and within $\sim$2 Myr its averaged surface rotational velocity drops below $350\,\mathrm{km\,s^{-1}}$. Close to the end of the main sequence, the internal transport of angular momentum causes a change in the spin-down slope.

Fig. 5 shows that, without accounting for the inclination angle, our model can retain a significant surface rotation for a time comparable to the kinematic age of the star, which is shorter than the remaining main-sequence lifetime. We emphasize that throughout its evolution this model is computed using the Vink et al. (2000, 2001) wind mass-loss rate with full efficiency. Marcolino et al. (2009) found the predicted mass loss rate to exceed the observed one by $\sim$2 orders of magnitude. While this could impact the evolution of the binary even before RLOF, it certainly increases the spin-down rate of our model compared to the observations. We attempted running models with artificially decreased wind mass loss rate (e.g., Renzo et al. 2017), but these resulted in super-critical $\omega/\omega_{\mathrm{crit}} > 1$ accretor stars with untrustworthy numerical results. Nevertheless, we expect that an accreting star modeled with lower wind-mass loss rate post-RLOF would retain an even higher surface rotation for longer.

3.2.1. *Comparison to single fast-rotating stars*

To illustrate the angular momentum transport in our accretor stars, it is helpful to compare with the single rotating $20\,M_\odot$ models. The internal rotational profile of a single star rigidly rotating at birth is different than the profile obtained spinning up the secondary star at a
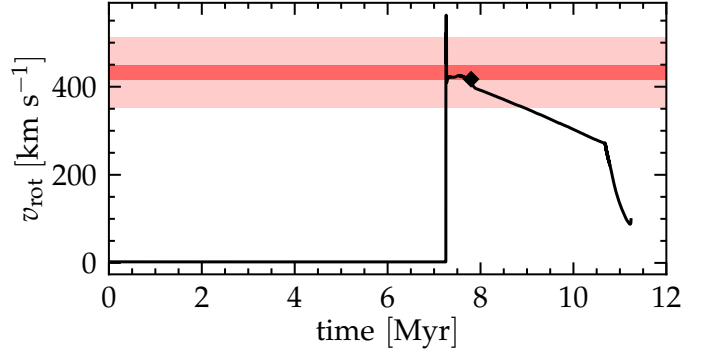
Figure 5. Surface averaged rotation rate for the accretor model. At $\sim$7.25 Myr the mass transfer quickly spins up the accretor at critical rotation. By the time the donor detaches from the RLOF the accretor is still spinning at $\sim$400 km s^{-1}. At this point (beginning of the dot-dashed line), we continue the evolution as a single star, and the accretor quickly spins down. Note however that we use a wind mass-loss rate from Vink et al. (2001), which is observed to be $\sim$2 orders of magnitude too high (Marcolino et al. 2009).

later evolutionary stage and from its surface. This even within the framework of a specific model for the angular momentum transport in stars (Spruit 2002).

Fig. 6 shows the internal equatorial rotational velocity $v_{\mathrm{rot}} = \omega \times r$. As in Fig. 4, the first four panels show single rotating stars with increasing initial $\omega/\omega_{\mathrm{crit}}$, the last panel shows our accretor model, and the colors go from dark (close to zero age main sequence, ZAMS) to light (TAMS), with the accretor reaching lighter colors because of its rejuvenation. The gray area in the last panel represents mass accreted during RLOF.

The thin dashed red lines in each panel mark the TAMS surface rotation rates: all our single star models reach a TAMS surface $v_{\mathrm{rot}} \simeq 50\,\mathrm{km\,s^{-1}}$. Initially faster rotating models spin down more in their outer layers, have slightly longer main sequence lifetimes (because of rotational mixing increasing the available fuel), and develop stronger differential rotation which drives more inwards transport of angular momentum. The single star profiles show the progressive development of a core-envelope interface, and the core rotation rate is sensitive to the initial value of $\omega/\omega_{\mathrm{crit}}$.

Conversely, the last panel shows that the entire interior of the accretor has a negligible equatorial rotational velocity until RLOF. Because of binary interactions, rotation does not start as rigid, but instead angular momentum is injected from the top. In our model, inward transport of angular momentum creates the monotonically increasing v_{rot} profile seen in the green lines of the last panel. When angular momentum is transported across the chemical gradient at the edge of the convec-

Figure 6. Internal rotational profile for 20 $M_\odot$ single star models with increasing $\omega/\omega_{\rm crit}$ at birth (first four panels), and for the accretor of our fiducial binary. As in Fig. 4, the colors go from dark (close to ZAMS) to light at TAMS, and the thin dashed red line mark the TAMS surface rotation rate. In the last panel, the gray area indicates mass accreted during RLOF. The yellow lines (TAMS) in the last panel show that the core of the accretor is rotating almost as fast as its surface, and both are faster than the surface of single star models.

tive core, a discontinuity stronger than in the single stars arises.

By the end of the main-sequence evolution of the accretor, the surface still spins with $v_{\rm rot} \simeq 100\,{\rm km\,s^{-1}}$ (twice as fast as the single star models). Perhaps more importantly, the outer-edge of the core has a similar rotational velocity as the surface, and much larger than the rotational velocity of the single star models. This might have important implications for the rotation rate of the compact objects formed by the initially less massive star in a binary, and the models of compact objects spins for gravitational-wave progenitors (e.g., Zaldarriaga et al. 2018; Qin et al. 2018; Callister et al. 2020).

4. ROBUSTNESS OF THE MODELS AND DISCUSSION

4.1. *Uncertainties in the treatment of mass transfer*

We regulate the accretion efficiency through the rotational enhancement of mass loss (e.g. Langer 1998). However, whether critical rotation can effectively stop the accretion of matter is still unclear. Popham & Narayan (1991) and Paczynski (1991) argued that accretion of mass (but no angular momentum) might be possible even at critical rotation.

During RLOF, the total amount of mass lost by the donor is $\Delta M_{\rm donor} \simeq 10.6\,M_\odot$, of which only $\Delta M_{\rm accretor} \simeq 3.4\,M_\odot$ are successfully accreted. This corresponds to an overall mass transfer efficiency $\beta_{\rm RLOF} \equiv \Delta M_{\rm accretor}/\Delta M_{\rm donor} \simeq 0.3$, although the accretion efficiency is *not* constant throughout the mass transfer (e.g., van Rensbergen et al. 2006), instead it depends on the radial and rotational evolution of the accreting star. In reality, the accretor will deviate from spherical simmetry because of centrifugal forces, and during the RLOF the accretor might be out of gravothermal equilibrium with significant impact on its radius and ultimately on the amount of mass transferred and its angular momentum.

While the mass transfer efficiency $\beta_{\rm RLOF}$ and importantly its time-evolution need further studies, we emphasize that most studies, especially using rapid population synthesis tools, typically assume a constant $\beta_{\rm RLOF}$ and neglect to model the out-of-equilibrium phase of the accretor and how this can impact the binary and orbital evolution.

Another free parameter in the treatment of mass transfer is the specific angular momentum of the accreted material. In our models, for the sake of numerical stability, we assume the incoming material and the stellar surface to have the same specific angular momentum. This approximation corresponds to a scenario where angular momentum transport in the circumstel-

lar disk during RLOF quickly homogenizes the rotation rate.

We also attempted calculations using the algorithm from de Mink et al. (2013) based on the fit from Ulrich & Burger (1976) to the numerical results of Lubow & Shu (1975). This algorithm distinguishes between direct impact of the L1 stream and circumstellar disk formation and determines the specific angular momentum of the incoming material. However, these models proved numerically more unstable and providing less trustworthy results. Generally speaking, allowing for a faster accretion of angular momentum results in less radial expansion of the accretor (cf. Fig. 1) and a lower overall mass transfer efficiency β_{RLOF} because of the faster achievement of critical rotation.

Finally, while the composition of the transferred material is determined by the structure of the donor and the mass transfer rate calculated following Kolb & Ritter (1990), we still need to specify its specific entropy when it reaches the accretor surface. We follow the common practice of assuming the specific entropy of the incoming material to be same as the accreting surface. The scenario justifying this hypothesis is that during RLOF the matter is sufficiently optically thin so radiative processes can rapidly equalize the entropy between the RLOF stream and the accreting surface. However, the very large mass-transfer rates we find (cf. Fig. 2) might result in optically thick flows for which this approximation might not be appropriate.

4.2. Uncertainties in the single-star physics

■ **[write about model variations]** ■

4.3. Variations in the initial binary parameters

■ **[discuss variations in M1, M2, P]** ■

4.4. The explosion of the former companion

Throughout this study, we have assumed the "binary SN scenario": after the mass transfer phase, the explosion of the donor breaks the binary and ejects the accretor with roughly its pre-explosion velocity (e.g., Renzo et al. 2019). This is the fate of the majority of massive binary systems, and ζ Oph might be the best example of this scenario (e.g., Blaauw 1952, 1961; Hoogerwerf et al. 2000). Neuhäuser et al. (2020) suggested not only the companion successfully exploded producing the pulsar PSR B1706-16, but that the explosion produced radioactive ^{60}Fe which polluted Earth. From kinematic and orbital considerations they estimated a natal kick of $\sim 253 \pm 54\,\mathrm{km\,s^{-1}}$, which would be sufficiently large to unbind the binary.

However, we have so far neglected the impact of the explosion on the structure of the accretor star. The blast wave will hit the companion at a ■ **[estimate solid angle]** ■ causing mass loss – directly via ablation and by injecting energy in the envelope, inflating it and enhancing its wind (Wheeler et al. 1975; Tauris & Takens 1998; Podsiadlowski 2003; Hirai et al. 2018).

Using 2D hydrodynamic simulations of the star-SN ejecta interactions in close binaries ($a \lesssim 60\,R_\odot$, cf. $a \gtrsim 343\,R_\odot$ in our fiducial binary model), Hirai et al. (2018) found that the companion star recovers its pre-explosion luminosity and effective temperature within a few years to decades, and the amount of mass removed by the SN shock is $\lesssim 10^{-2}\,M_\odot$

■ **[estimate mass loss]** ■

Because of the SN shock, the just ejected new runaway star might appear bloated and redder (long before it overtakes the slowing SN remnant). The impact of this brief out of thermal equilibrium phase on the stellar spin should be investigated further.

The SN ejecta might also pollute the surface of the runaway depositing processed nuclear material (e.g. Przybilla et al. 2008). However, enhahnced mass loss, rapid rotation and mixing might rapidly dilute the yields.

5. CONCLUSIONS

We have demonstrated that self-consistent one-dimensional calculations of coupled stellar models with masses $\gtrsim 20\,M_\odot$ are possible with the MESA software instrument. As a first application, we focused on finding a model for ζ Oph, assuming its runaway nature is explained by the binary SN scenario.

We found that it is likely possible to explain its surface composition without assuming that the surface excess of He and N comes from within the star. Instead, this material comes from the receding core of the donor star. Therefore, the present day abundances constrain the accretion efficiency and mixing in the accretor.

ζ Oph should therefore *not* be used to test models of rotational mixing in single star evolution, nor its more extreme version of chemically homogeneous evolution.

ACKNOWLEDGMENTS

APPENDIX

A. MESA SETUP

■ [MLT−?] ■

■ [possibly move to methods] ■ We use MESA version 15140 to compute our models. The MESA equation of state (EOS) is a blend of the OPAL Rogers & Nayfonov (2002), SCVH Saumon et al. (1995), PTEH Pols et al. (1995), HELM Timmes & Swesty (2000), and PC Potekhin & Chabrier (2010) EOSes.

OPAL (Iglesias & Rogers 1993, 1996) provides the main radiative opacities, with low-temperature data from Ferguson et al. (2005) and the high-temperature from Buchler & Yueh (1976). Electron conduction opacities are from Cassisi et al. (2007).

Nuclear reaction rates are a combination of rates from NACRE (Angulo et al. 1999), JINA REACLIB (Cyburt et al. 2010), plus additional tabulated weak reaction rates Fuller et al. (1985); Oda et al. (1994); Langanke & Martínez-Pinedo (2000). Screening is included via the prescription of Chugunov et al. (2007). Thermal neutrino loss rates are from Itoh et al. (1996). We use a 22-isotope nuclear network (approx_21_plus_cr56).

The inlists, processing scripts, and model output will be made available at link.

B. RESOLUTION TESTS

We extensively check the numerical convergence of our stellar evolution calculations with increasing number of mesh points. Fig. 7 shows that all the features described extensively here do not vary when increasing the spatial resolution by decreasing mesh_delta_coeff. The right panel shows the number of mesh points for the accretor (top) and donor (bottom), which are $\sim 20\%$ higher in the high resolution runs. The left panel shows the HRD evolution until the detachment of the binary for the two accretor models (pink/red) and the two donor models (blue/cyan).

Similarly, we tested the numerical convergence with decreasing timestep size. This can be done decreasing the parameter mesh_time_coeff. However, we were unable to successfully compute models at higher temporal resolution. Partial results show a good agreement with our fiducial model until they crash (typically during RLOF), and lower temporal resolution models showed a similar qualitative agreement but increased noisiness during the late RLOF phase. For our fiducial model the adaptive timestep size never exceeds $10^{3.8}$ years with typical pre-RLOF timesteps of the order of $10^{3.2}$ years and sub-decade during RLOF. The main factor limiting the timestep sizes is the change of surface angular momentum in both stars during the mass transfer.

REFERENCES

Almeida, L. A., Sana, H., Taylor, W., et al. 2017, A&A, 598, A84, doi: 10.1051/0004-6361/201629844

Angulo, C., Arnould, M., Rayet, M., et al. 1999, Nuclear Physics A, 656, 3, doi: 10.1016/S0375-9474(99)00030-5

Belczynski, K., Holz, D. E., Bulik, T., & O'Shaughnessy, R. 2016, Nature, 534, 512, doi: 10.1038/nature18322

Blaauw, A. 1952, BAN, 11, 414

—. 1961, BAN, 15, 265

Blaauw, A. 1993, in Astronomical Society of the Pacific Conference Series, Vol. 35, Massive Stars: Their Lives in the Interstellar Medium, ed. J. P. Cassinelli & E. B. Churchwell, 207

Blagorodnova, N., Klencki, J., Pejcha, O., et al. 2021, arXiv e-prints, arXiv:2102.05662. https://arxiv.org/abs/2102.05662

Bodensteiner, J., Baade, D., Greiner, J., & Langer, N. 2018, A&A, 618, A110, doi: 10.1051/0004-6361/201832722

Braun, H., & Langer, N. 1995, A&A, 297, 483

Broekgaarden, F. S., Berger, E., Neijssel, C. J., et al. 2021, arXiv e-prints, arXiv:2103.02608. https://arxiv.org/abs/2103.02608

Brott, I., de Mink, S. E., Cantiello, M., et al. 2011, A&A, 530, A115, doi: 10.1051/0004-6361/201016113

Buchler, J. R., & Yueh, W. R. 1976, ApJ, 210, 440, doi: 10.1086/154847

Callister, T. A., Farr, W. M., & Renzo, M. 2020, arXiv e-prints, arXiv:2011.09570. https://arxiv.org/abs/2011.09570

Cantiello, M., Lecoanet, D., Jermyn, A. S., & Grassitelli, L. 2021, arXiv e-prints, arXiv:2102.05670. https://arxiv.org/abs/2102.05670

Cantiello, M., Yoon, S., Langer, N., & Livio, M. 2007, A&A, 465, L29

Cassisi, S., Potekhin, A. Y., Pietrinferni, A., Catelan, M., & Salaris, M. 2007, ApJ, 661, 1094, doi: 10.1086/516819
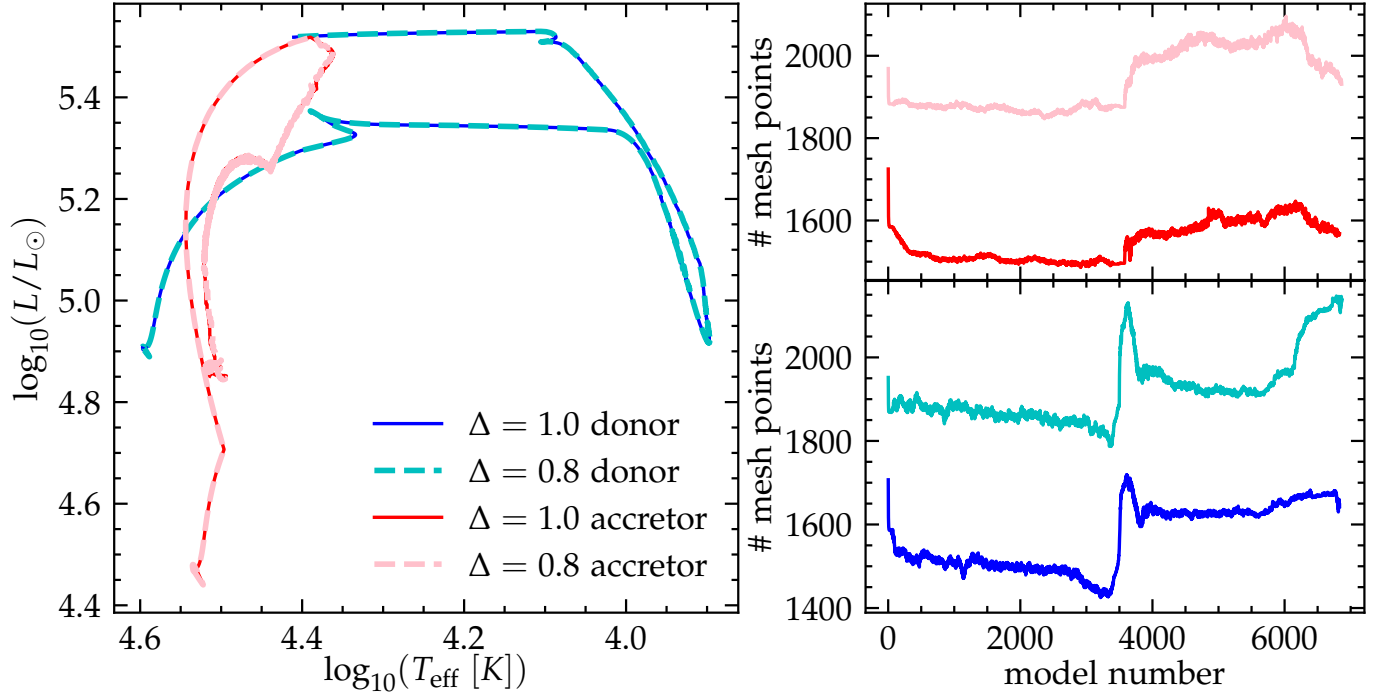
Figure 7. Left: HRD comparison for our fiducial binary model varying the number of mesh points. We only show the evolution until our definition of RLOF detachment. Right: number of mesh points as a function of timestep number. In both panels, the blue/cyan tracks show the donor stars, the red/pink tracks show the accretor. Thicker dashed lines correspond to the models at higher resolution (i.e., lower Δ which indicates the value of `mesh_delta_coeff`).

Chugunov, A. I., Dewitt, H. E., & Yakovlev, D. G. 2007, PhRvD, 76, 025028, doi: 10.1103/PhysRevD.76.025028

Claret, A., & Torres, G. 2017, ApJ, 849, 18, doi: 10.3847/1538-4357/aa8770

Cyburt, R. H., Amthor, A. M., Ferguson, R., et al. 2010, ApJS, 189, 240, doi: 10.1088/0067-0049/189/1/240

De Donder, E., Vanbeveren, D., & van Bever, J. 1997, A&A, 318, 812

de Jager, C., Nieuwenhuijzen, H., & van der Hucht, K. A. 1988, A&AS, 72, 259

de Mink, S. E., Langer, N., Izzard, R. G., Sana, H., & de Koter, A. 2013, ApJ, 764, 166, doi: 10.1088/0004-637X/764/2/166

Eldridge, J. J., Langer, N., & Tout, C. A. 2011, MNRAS, 414, 3501, doi: 10.1111/j.1365-2966.2011.18650.x

Evans, F. A., Renzo, M., & Rossi, E. M. 2020, arXiv e-prints, arXiv:2006.00849. https://arxiv.org/abs/2006.00849

Farmer, R. 2018, rjfarmer/mesaplot, doi: 10.5281/zenodo.1441329

Ferguson, J. W., Alexander, D. R., Allard, F., et al. 2005, ApJ, 623, 585, doi: 10.1086/428642

Fuller, G. M., Fowler, W. A., & Newman, M. J. 1985, ApJ, 293, 1, doi: 10.1086/163208

Götberg, Y., de Mink, S. E., & Groh, J. H. 2017. https://arxiv.org/abs/1701.07439

Götberg, Y., de Mink, S. E., Groh, J. H., et al. 2018, A&A, 615, A78, doi: 10.1051/0004-6361/201732274

Grevesse, N., & Sauval, A. J. 1998, SSRv, 85, 161, doi: 10.1023/A:1005161325181

Heger, A., Langer, N., & Woosley, S. E. 2000, ApJ, 528, 368

Hellings, P. 1983, Ap&SS, 96, 37, doi: 10.1007/BF00661941

—. 1984, Ap&SS, 104, 83, doi: 10.1007/BF00653994

Herrero, A., Kudritzki, R. P., Vilchez, J. M., et al. 1992, A&A, 261, 209

Herwig, F. 2000, A&A, 360, 952

Hirai, R., Podsiadlowski, P., & Yamada, S. 2018. https://arxiv.org/abs/1803.10808

Hoogerwerf, R., de Bruijne, J. H. J., & de Zeeuw, P. T. 2000, ApJL, 544, L133, doi: 10.1086/317315

—. 2001, A&A, 365, 49, doi: 10.1051/0004-6361/20000014

Hunter, J. D. 2007, Computing In Science & Engineering, 9, 90

Iglesias, C. A., & Rogers, F. J. 1993, ApJ, 412, 752, doi: 10.1086/172958

—. 1996, ApJ, 464, 943, doi: 10.1086/177381

Itoh, N., Hayashi, H., Nishikawa, A., & Kohyama, Y. 1996, ApJS, 102, 411, doi: 10.1086/192264

Kippenhahn, R., Ruschenplatt, G., & Thomas, H.-C. 1980, A&A, 91, 175

Kippenhahn, R., & Weigert, A. 1967, ZA, 65, 251

Klencki, J., Nelemans, G., Istrate, A. G., & Chruslinska, M. 2021, A&A, 645, A54, doi: 10.1051/0004-6361/202038707

Kolb, U., & Ritter, H. 1990, A&A, 236, 385

Lagae, C., Driessen, F. A., Hennicker, L., Kee, N. D., & Sundqvist, J. O. 2021, arXiv e-prints, arXiv:2103.15904. https://arxiv.org/abs/2103.15904

Langanke, K., & Martínez-Pinedo, G. 2000, Nuclear Physics A, 673, 481, doi: 10.1016/S0375-9474(00)00131-7

Langer, N. 1998, A&A, 329, 551

Langer, N., Fricke, K. J., & Sugimoto, D. 1983, A&A, 126, 207

Laplace, E., Götberg, Y., de Mink, S. E., Justham, S., & Farmer, R. 2020, A&A, 637, A6, doi: 10.1051/0004-6361/201937300

Laplace, E., Justham, S., Renzo, M., et al. 2021, arXiv e-prints, arXiv:2102.05036. https://arxiv.org/abs/2102.05036

Law-Smith, J. A. P., Everson, R. W., Ramirez-Ruiz, E., et al. 2020, arXiv e-prints, arXiv:2011.06630. https://arxiv.org/abs/2011.06630

Lubow, S. H., & Shu, F. H. 1975, ApJ, 198, 383, doi: 10.1086/153614

Lucy, L. B. 2012, A&A, 544, A120, doi: 10.1051/0004-6361/201118753

Maeder, A., & Meynet, G. 2000, ARA&A, 38, 143, doi: 10.1146/annurev.astro.38.1.143

Marcolino, W. L. F., Bouret, J. C., Martins, F., et al. 2009, A&A, 498, 837, doi: 10.1051/0004-6361/200811289

Mason, B. D., Hartkopf, W. I., Gies, D. R., Henry, T. J., & Helsel, J. W. 2009, AJ, 137, 3358, doi: 10.1088/0004-6256/137/2/3358

Meynet, G., & Maeder, A. 2000, A&A, 361, 101

Murphy, S. J., Joyce, M., Bedding, T. R., White, T. R., & Kama, M. 2021, MNRAS, 502, 1633, doi: 10.1093/mnras/stab144

Neo, S., Miyaji, S., Nomoto, K., & Sugimoto, D. 1977, PASJ, 29, 249

Neuhäuser, R., Gießler, F., & Hambaryan, V. V. 2020, MNRAS, 498, 899, doi: 10.1093/mnras/stz2629

Oda, T., Hino, M., Muto, K., Takahara, M., & Sato, K. 1994, Atomic Data and Nuclear Data Tables, 56, 231, doi: 10.1006/adnd.1994.1007

Packet, W. 1981, A&A, 102, 17

Paczynski, B. 1991, ApJ, 370, 597, doi: 10.1086/169846

Paxton, B., Bildsten, L., Dotter, A., et al. 2011, ApJS, 192, 3, doi: 10.1088/0067-0049/192/1/3

Paxton, B., Cantiello, M., Arras, P., et al. 2013, ApJS, 208, 4, doi: 10.1088/0067-0049/208/1/4

Paxton, B., Marchant, P., Schwab, J., et al. 2015, ApJS, 220, 15, doi: 10.1088/0067-0049/220/1/15

Paxton, B., Schwab, J., Bauer, E. B., et al. 2018, ApJS, 234, 34, doi: 10.3847/1538-4365/aaa5a8

Paxton, B., Smolec, R., Gautschy, A., et al. 2019. https://arxiv.org/abs/1903.01426

Pérez, F., & Granger, B. E. 2007, Computing in Science & Engineering, 9, 21

Perna, R., Duffell, P., Cantiello, M., & MacFadyen, A. I. 2014, ApJ, 781, 119, doi: 10.1088/0004-637X/781/2/119

Podsiadlowski, P. 2003, arXiv e-prints, astro. https://arxiv.org/abs/astro-ph/0303660

Pols, O. R., & Marinus, M. 1994, A&A, 288, 475

Pols, O. R., Tout, C. A., Eggleton, P. P., & Han, Z. 1995, MNRAS, 274, 964, doi: 10.1093/mnras/274.3.964

Popham, R., & Narayan, R. 1991, ApJ, 370, 604, doi: 10.1086/169847

Potekhin, A. Y., & Chabrier, G. 2010, Contributions to Plasma Physics, 50, 82, doi: 10.1002/ctpp.201010017

Przybilla, N., Nieva, M. F., Heber, U., & Butler, K. 2008, The Astrophysical Journal, 684, L103, doi: 10.1086/592245

Qin, Y., Fragos, T., Meynet, G., et al. 2018, A&A, 616, A28, doi: 10.1051/0004-6361/201832839

Renzo, M., Ott, C. D., Shore, S. N., & de Mink, S. E. 2017, A&A, 603, A118, doi: 10.1051/0004-6361/201730698

Renzo, M., Zapartas, E., de Mink, S. E., et al. 2019, A&A, 624, A66, doi: 10.1051/0004-6361/201833297

Rogers, F. J., & Nayfonov, A. 2002, ApJ, 576, 1064, doi: 10.1086/341894

Sana, H., de Mink, S. E., de Koter, A., et al. 2012, Science, 337, 444, doi: 10.1126/science.1223344

Saumon, D., Chabrier, G., & van Horn, H. M. 1995, ApJS, 99, 713, doi: 10.1086/192204

Schneider, F. R. N., Podsiadlowski, P., Langer, N., Castro, N., & Fossati, L. 2016, MNRAS, 457, 2355, doi: 10.1093/mnras/stw148

Schneider, F. R. N., Podsiadlowski, P., & Müller, B. 2021, A&A, 645, A5, doi: 10.1051/0004-6361/202039219

Sota, A., Maíz Apellániz, J., Morrell, N. I., et al. 2014, ApJS, 211, 10, doi: 10.1088/0067-0049/211/1/10

Spruit, H. C. 2002, A&A, 381, 923, doi: 10.1051/0004-6361:20011465

Sweet, P. A. 1950, MNRAS, 110, 548, doi: 10.1093/mnras/110.6.548

Tauris, T. M. 2015, MNRAS, 448, L6, doi: 10.1093/mnrasl/slu189

Tauris, T. M., & Takens, R. J. 1998, A&A, 330, 1047

Tauris, T. M., Kramer, M., Freire, P. C. C., et al. 2017, ApJ, 846, 170, doi: 10.3847/1538-4357/aa7e89

Tetzlaff, N., Neuhäuser, R., Hohle, M. M., & Maciejewski, G. 2010, MNRAS, 402, 2369, doi: 10.1111/j.1365-2966.2009.16093.x

Timmes, F. X., & Swesty, F. D. 2000, ApJS, 126, 501, doi: 10.1086/313304

Townsend, R. 2018, MESA SDK for Linux: 20180822, doi: 10.5281/zenodo.2603170

Ulrich, R. K., & Burger, H. L. 1976, ApJ, 206, 509, doi: 10.1086/154406

van der Walt, S., Colbert, S. C., & Varoquaux, G. 2011, Computing in Science Engineering, 13, 22, doi: 10.1109/MCSE.2011.37

van Rensbergen, W., de Greve, J. P., Mennekens, N., Jansen, K., & de Loore, C. 2011, A&A, 528, A16, doi: 10.1051/0004-6361/201015596

van Rensbergen, W., De Loore, C., & Jansen, K. 2006, A&A, 446, 1071, doi: 10.1051/0004-6361:20053543

van Rensbergen, W., Vanbeveren, D., & De Loore, C. 1996, A&A, 305, 825

Villamariz, M. R., & Herrero, A. 2005, A&A, 442, 263, doi: 10.1051/0004-6361:20052848

Vink, J. S., Davies, B., Harries, T. J., Oudmaijer, R. D., & Walborn, N. R. 2009, A&A, 505, 743, doi: 10.1051/0004-6361/200912610

Vink, J. S., de Koter, A., & Lamers, H. J. G. L. M. 2000, A&A, 362, 295

—. 2001, A&A, 369, 574, doi: 10.1051/0004-6361:20010127

Walker, G. A. H., Yang, S., & Fahlman, G. G. 1979, ApJ, 233, 199, doi: 10.1086/157381

Wang, C., Langer, N., Schootemeijer, A., et al. 2020, ApJL, 888, L12, doi: 10.3847/2041-8213/ab6171

Wheeler, J. C., Lecar, M., & McKee, C. F. 1975, ApJ, 200, 145, doi: 10.1086/153771

Yoon, S.-C., Langer, N., & Norman, C. 2006, A&A, 460, 199, doi: 10.1051/0004-6361:20065912

Zaldarriaga, M., Kushnir, D., & Kollmeier, J. A. 2018, MNRAS, 473, 4174, doi: 10.1093/mnras/stx2577

Zapartas, E., de Mink, S. E., Justham, S., et al. 2021, A&A, 645, A6, doi: 10.1051/0004-6361/202037744

—. 2019. https://arxiv.org/abs/1907.06687

Zehe, T., Mugrauer, M., Neuhäuser, R., et al. 2018, Astronomische Nachrichten, 339, 46, doi: 10.1002/asna.201713383